UCLA
UCLA Previously Published Works

Title

Common fibrillar spines of amyloid-β and human islet amyloid polypeptide revealed by microelectron diffraction and structure-based inhibitors

Permalink

Journal

ISSN

Authors

Krotee, Pascal
Griner, Sarah L
Sawaya, Michael R
et al.

Publication Date

DOI

Peer reviewed

Common fibrillar spines of amyloid-β and human islet amyloid polypeptide revealed by microelectron diffraction and structure-based inhibitors

Pascal Krotee[‡1], Sarah L. Griner[‡1], Michael R. Sawaya[‡], Duilio Cascio[‡], Jose A. Rodriguez[‡], Dan Shi[§], Stephan Philipp[¶], Kevin Murray[‡], Lorena Saelices[‡], Ji Lee[‡], Paul Seidler[‡], Charles G. Glabe[¶‖], Lin Jiang[**], Tamir Gonen[§], and David S. Eisenberg[‡2]

From the ‡Howard Hughes Medical Institute, UCLA-United States Department of Energy (DOE) Institute, Departments of Biological Chemistry and Chemistry and Biochemistry, Molecular Biology Institute, UCLA, Los Angeles, California 90095, §Howard Hughes Medical Institute, Janelia Research Campus, Ashburn, Virginia 20147, ¶Department of Molecular Biology and Biochemistry, University of California, Irvine, California 92697, ‖Biochemistry Department, Faculty of Science and Experimental Biochemistry Unit, King Fahd Medical Research Center, King Abdulaziz University, Jeddah 22252, Saudi Arabia, and **Department of Neurology, Molecular Biology Institute, and Brain Research Institute (BRI), David Geffen School of Medicine, UCLA, Los Angeles, California, 90095

Edited by Paul E. Fraser

Amyloid-β (Aβ) and human islet amyloid polypeptide (hIAPP) aggregate to form amyloid fibrils that deposit in tissues and are associated with Alzheimer's disease (AD) and type II diabetes (T2D), respectively. Individuals with T2D have an increased risk of developing AD, and conversely, AD patients have an increased risk of developing T2D. Evidence suggests that this link between AD and T2D might originate from a structural similarity between aggregates of Aβ and hIAPP. Using the cryoEM method microelectron diffraction, we determined the atomic structures of 11-residue segments from both Aβ and hIAPP, termed Aβ(24–34) WT and hIAPP(19–29) S20G, with 64% sequence similarity. We observed a high degree of structural similarity between their backbone atoms (0.96-Å root mean square deviation). Moreover, fibrils of these segments induced amyloid formation through self- and cross-seeding. Furthermore, inhibitors designed for one segment showed cross-efficacy for full-length Aβ and hIAPP and reduced cytotoxicity of both proteins, although by apparently blocking different cytotoxic mechanisms. The similarity of the atomic structures of Aβ(24–34) WT and hIAPP(19–29) S20G offers a molecular model for cross-seeding between Aβ and hIAPP.

Amyloid fibrils are protein aggregates associated with pathogenesis in a variety of incurable, and largely untreatable, diseases. These fibrils all appear morphologically similar and share β-sheet–rich structures, which stack along the fibril axis. Such fibrils give a cross-β diffraction pattern when they are aligned and analyzed in an X-ray or electron beam (1–3). Two of the most prevalent of these amyloid diseases are Alzheimer's disease (AD)[3] and type II diabetes (T2D). In AD, extracellular amyloid fibrils that form senile plaques are composed of amyloid-β (Aβ), a peptide of 39–42 amino acids. In T2D, amyloid fibrils are composed of human islet amyloid polypeptide (hIAPP), a 37-amino acid peptide hormone (4, 5).

Although, as far as is known, each fibril is composed of a single protein, the deposits can contain fibrils of more than one protein, which has led to the hypothesis that amyloid proteins may make cross-sequence interactions as well as self-assemble (6). For example, in AD, Aβ has been reported to form soluble complexes with tau (7) as well as codeposit with α-synuclein (8) and transthyretin (9), whereas hIAPP aggregation is inhibited by binding to insulin (10, 11). Recently, hIAPP has been found to codeposit with Aβ in senile plaques in AD patient–derived samples (12).

The codeposition of Aβ and hIAPP might arise from cross-seeding events where fibrils of one sequence lower the energy barrier to fibrilization of the other sequence. The molecular mechanism of cross-seeding is unknown but likely depends on structural similarity between aggregates of the two proteins. In the native state, both proteins are unfolded but contain hydrophobic regions that are highly aggregation-prone. Their sequences are 50% similar and 25% identical (Fig. 1A) with sequence segments important for self-aggregation displaying the greatest similarity (13). Protein segments of hIAPP and Aβ

[3] The abbreviations used are: AD, Alzheimer's disease; T2D, type II diabetes; Aβ, amyloid-β; hIAPP, human islet amyloid polypeptide; mIAPP, mouse islet amyloid polypeptide; microED, microelectron diffraction; N2a, Neuro-2a; ThT, thioflavin-T; Sc, shape complementarity; MTT, 3-(4,5-dimethylthiazol-2-yl)-2,5-diphenyltetrazolium bromide; r.m.s.d., root mean square deviation; TEM, transmission electron microscopy; HFIP, 1,1,1,3,3,3-hexafluoro-2-propanol; ANOVA, analysis of variance.
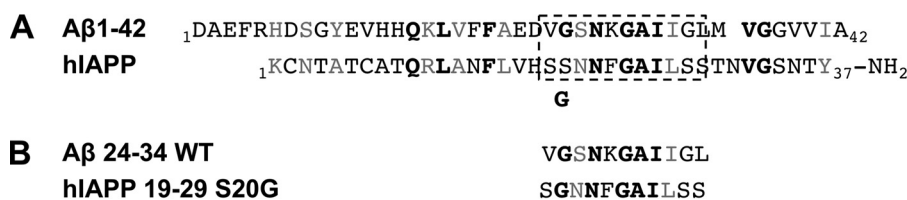
A **Aβ1-42** $_1$DAEF**R**HDSGYEVHH**Q**K**L**VF**F**AED|**VGSNKGAI**IG**L**M **VG**GVVIA$_{42}$

hIAPP $_1$KCNTATCAT**Q**RLAN**F**LVH|SSN**NFGAIL**SS|TN**VG**SNTY$_{37}$–NH$_2$

G

B **Aβ 24-34 WT** **VGS**N**K**GA**I**IGL

hIAPP 19-29 S20G **SGN**N**F**GA**I**LSS

Figure 1. Sequence alignment of Aβ(1–42) and hIAPP. Identical residues are highlighted in *bold font* and similar residues are highlighted in *gray*. *A*, alignment of Aβ(1–42) and hIAPP sequences reveals that hIAPP is 51% similar and 27% identical to Aβ(1–42). The early-onset type II diabetes mutation in hIAPP, S20G, is shown below the hIAPP sequence. The amyloid spines of Aβ(1–42) and hIAPP are *boxed* with *dotted lines*. hIAPP S20G was used to calculate sequence similarity to Aβ(1–42). *B*, alignment of the spine segments Aβ(24–34) WT and hIAPP(19–29) S20G reveals that they are 64% similar and 45% identical.

with the highest similarity bind to one another with high affinity (14, 15) and appear to catalyze heteroassembly. Aβ and hIAPP appear to interact not only in their native unfolded states but also can interact once aggregated. Aβ fibrils cross-seed hIAPP fibril formation, suggesting that the 3D fibril structure of Aβ is able to template hIAPP aggregation, possibly by conferring a similar structural motif (16). Supporting the idea that the underlying structures of the fibrils are similar, a recent study describes a peptide-based fibril blocker that mitigates fibril formation and cytotoxicity of both Aβ and hIAPP (17).

Cross-seeding is further evident in *in vivo* studies. One study showed that islet amyloid formed in hIAPP transgenic mice upon injection with fibril seeds of either Aβ or hIAPP (12). Moreover, a recent study observed a similar cross-seeding effect when Aβ transgenic mice were injected with hIAPP seeds (18). Beyond model systems, clinical studies have reported increased risk for AD in T2D patients and vice versa (19–21). Some studies suggest AD and T2D are connected by heightened stress and cholesterol levels, whereas others propose that cross-amyloid interactions, or cross-seeding, connect the diseases (22). This has led some to hypothesize that drugs used to treat T2D may be effective treatments for AD (23).

In an effort to uncover a molecular basis for interaction of Aβ with hIAPP, we focused on two 11-residue, fibril-forming protein segments with 64% sequence identity; we call these segments Aβ(24–34) WT and hIAPP(19–29) S20G, which harbors a familial mutation implicated in early-onset T2D (Fig. 1B) (24–26). In addition to high identity, these sequences appear to be important for aggregation and accompanying toxicity of their respective full-length proteins. The Aβ(24–34) WT segment is integral to the core in structures of full-length Aβ fibrils as determined from solid-state NMR (27–30). Additionally, short peptides spanning from residues 27 to 32 and 29 to 34 of Aβ crystallize in steric zipper arrangements (31). Aβ(24–34) WT contains residues necessary for oligomerization and formation of toxic species (32–34). Previously, we demonstrated that fibrils formed from the hIAPP(19–29) S20G segment are structurally related to those of full-length hIAPP and comprise the spine of the mature fibrils (35). Thus, Aβ(24–34) WT and hIAPP(19–29) S20G are candidates for self- and cross-interacting segments of their two parent proteins.

Results

Atomic structure of Aβ(24–34) WT determined using microelectron diffraction (microED)

Aβ(24–34) WT crystallized as nanocrystals only a few hundred nanometers thick (Fig. 2A), similar to the 11-residue seg-

ments of previously determined amyloid structures (3, 35). This crystal size is ideal for microED, a diffraction mode of cryoEM (36–39).

The structure of Aβ(24–34) WT reveals a class I steric zipper with pairs of parallel in-register β-sheets antiparallel to each other (Fig. 2B and Table 1). The side chains interdigitate to form two dry interfaces (Fig. S1). Interface A buries 210 Å^2 of solvent-accessible surface area per strand with a shape complementarity (Sc) of 0.62 with Ala^{30}, Ile^{32}, and Leu^{34} lining the zipper interface. Additionally, this interface is capped by hydrogen bonding of Lys^{28} to the carboxyl terminus of the opposing sheet. Interface B is somewhat larger; it buries 256 Å^2 of solvent-accessible surface area and has an Sc of 0.85 with Asn^{27}, Gly^{29}, and Ile^{31} lining the center of the interface. Flanking this interface, Val^{24} packs into the space provided by the lack of side chain at Gly^{33}, and salt bridges form between terminal amine and carboxylates from opposing sheets as previously seen in the non-amyloid-β component core (NACore) of α-synuclein (3). These latter two interactions are introduced by a kink at Gly^{25}.

There are similarities in the fibril diffraction patterns of Aβ(1–42) and our crystallized segment. Both display meridional reflections at spacings of 4.7 and 2.4 Å, indicative of the strand-strand spacing within β-sheets, and a set of reflections around 3.7 Å (Fig. 2C). The diffraction pattern of Aβ(24–34) WT has two strong equatorial reflections at 8.6 and 7.4 Å, which match the average separations of the β-sheets in Interfaces A and B, respectively. The closest corresponding reflections in the Aβ(1–42) diffraction pattern are centered around 10 Å, which matches more closely with Interface A rather than B. We hypothesize that Interface A contributes to the strength and spacing of this reflection and therefore is part of the spine of Aβ(1–42) fibrils.

Segment Aβ(24–34) WT is cytotoxic

Full-length Aβ is known to be cytotoxic (40), and we wondered whether the segment Aβ(24–34) WT could be the source of this cytotoxicity. To investigate the cytotoxicity of Aβ(24–34) WT, we assessed the effects of the soluble and fibrillar forms of the protein segment on Neuro-2a (N2a) cells, a mouse neuroblastoma cell line (41). We measured cytotoxicity using 3-(4,5-dimethylthiazol-2-yl)-2,5-diphenyltetrazolium bromide (MTT) dye reduction (42, 43), and we measured proapoptotic caspase activation using a fluorescent marker for caspase activity.

MTT dye reduction assays revealed that soluble Aβ(24–34) WT is mildly cytotoxic at high concentrations, but its fibrillar form is significantly more cytotoxic (Fig. 3A). Aβ(24–34) WT is
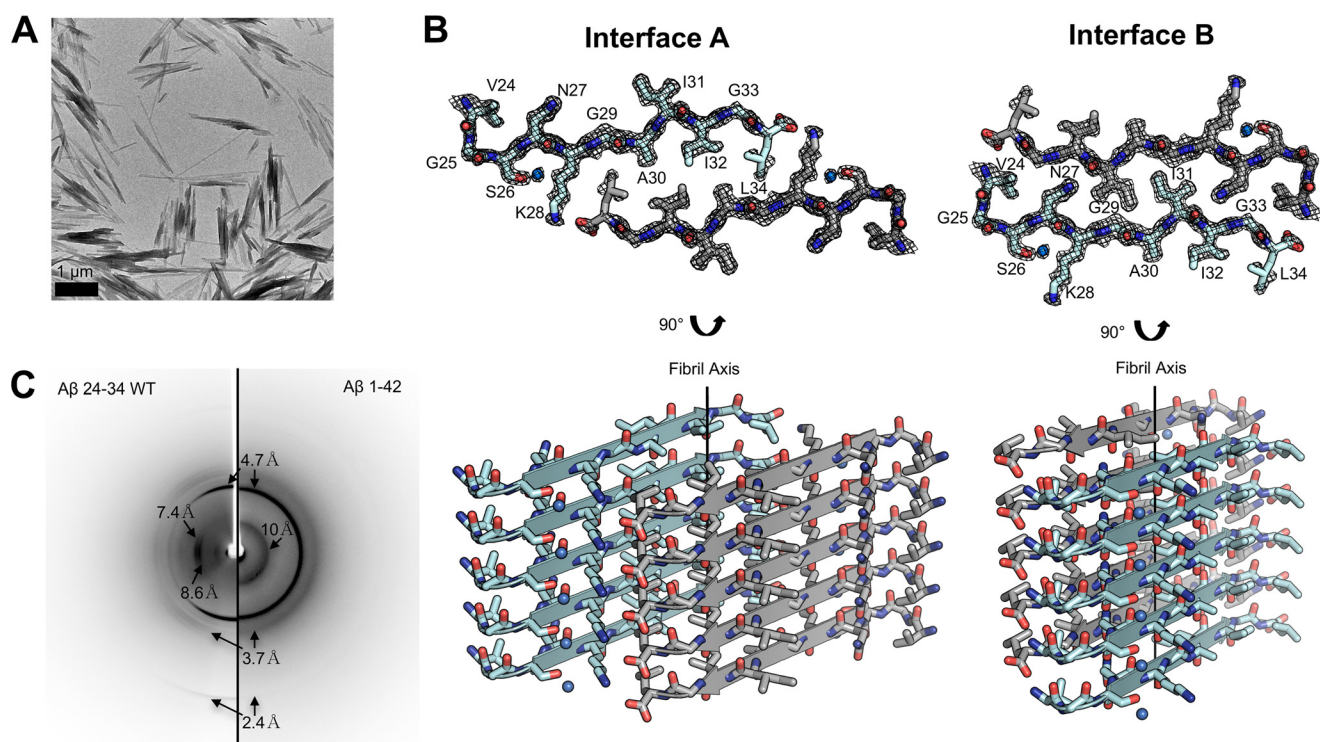
Figure 2. MicroED structure of segment Aβ(24–34) WT from microcrystals. *A*, electron micrograph of 3D crystals used for data collection. *B*, the crystal structure reveals tightly mated pairs of β-sheets. The side chains interdigitate to form two extensive dry interfaces, termed Interface A and Interface B. *Top*, one layer viewed down the fibril axes with the $2F_o - F_c$ electron density at 1σ displayed as *black mesh*. *Bottom*, six layers viewed nearly perpendicular to the fibril axis. The β-sheets are related by a 2_1 axis parallel to the fibril axis. *C*, comparison of the fibril diffraction of aligned Aβ(24–34) WT microcrystals and Aβ(1–42). Both display a strong reflection at a spacing of 4.7 Å and a weaker reflection at 2.4 Å. Additionally, the two have a broad reflection around 3.7 Å. Aβ(24–34) WT has two distinct reflections at 8.6 and 7.4 Å, reflecting the separation of β-sheets in each interface, whereas Aβ(1–42) has a broad reflection around 10 Å.

not as cytotoxic as full-length Aβ(1–42), possibly because Aβ(24–34) WT lacks other residues that are important for cytotoxicity, particularly Met[35], which is an important contributor to the potent cytotoxicity of Aβ(25–35) (44, 45). Additionally, we observed that fibrillar Aβ(24–34) WT activates proapoptotic caspases but to a lesser degree than full-length Aβ(1–42) at similar concentrations (Fig. 3*B* and Fig. S2). Fibrils of the toxic spine from hIAPP, hIAPP(19–29) S20G, are slightly more cytotoxic than Aβ(24–34) WT to the same cell line (Fig. S2).

The insoluble fraction of the Aβ(24–34) WT fibrillar sample is cytotoxic, whereas the soluble fractions are not, thus suggesting that fibrils are the cytotoxic species (Fig. 3*B*). However, it is plausible that some undetectable population of highly toxic oligomers that associate with fibrils causes the cytotoxicity of the fibrillar sample.

The spines of Aβ and hIAPP are structurally similar

The similarity in sequence between segments Aβ(24–34) WT and hIAPP(19–29) S20G motivated us to compare their atomic structures. We had previously applied microED to determine the atomic structure of hIAPP(19–29) S20G (35), a spine segment of hIAPP 64% similar in sequence to Aβ(24–34) WT (Fig. 1*B*).

For both segments, the crystal reveals two sheet-to-sheet interfaces termed Interface A and Interface B, described previously for the structure of Aβ(24–34) WT (Fig. 4*A*). In the crystal structure of hIAPP(19–29) S20G, Interface A is lined by Asn[21], Phe[23], Ala[25], and Leu[27], whereas residues Asn[22], Gly[24], Ile[26], and Ser[28] line Interface B. Interface A of hIAPP(19–29)

S20G is likely the primary interface because it excludes waters, and fibril diffraction calculated from this interface best matches diffraction collected from full-length hIAPP fibrils. Its Interface B contains waters and has lower shape complementarity. The primary interface of Aβ(24–34) WT is less clear; both its A and B interfaces are dry and large. Either could exist in Aβ(1–42); although interface B appears somewhat stronger, interface A is closer to observed diffraction of the full-length fibers.

Our structures reveal a similarity that is not accurately reflected by their sequence similarity. We observed that the two A interfaces are more structurally similar to each other than the two Interfaces B. Superimposing Aβ(24–34) WT onto hIAPP(19–29) S20G using LSQKAB, we found that backbone atoms of the A interfaces superimpose with 0.96-Å root mean square deviation (r.m.s.d.) (Fig. 4*A*), and the backbones of the B interfaces superimpose with a higher r.m.s.d. of 2.11 Å. Surprisingly, the structural alignment with lower r.m.s.d. (Interfaces A) has fewer sequence equivalences than structural alignment with higher r.m.s.d. (Interfaces B). That is, residues expected to align by sequence identity are shifted by two residues in the structural alignment of Interfaces A (Fig. 4*B*). Although Ala[30] in Aβ(24–34) WT would be expected to align with Ala[25] in hIAPP(19–29) S20G, the structural alignment instead superimposes these alanines with Phe[23] in hIAPP and Ile[32] in Aβ, respectively. Moreover, the leucines in the cores of each of the two interfaces, which are not paired in the sequence alignment, almost perfectly superimpose. This startling result makes one

Table 1
Statistics of microED data collection and atomic refinement
r.m.s., root mean square; Avg., average.

	VGSNKGAIIGL
Data collection	
Excitation voltage (kV)	200
Electron source	Field emission gun
Wavelength (Å)	0.0251
Total dose per crystal (e^-/Å^2)	2.7
Frame rate (frame/s)	0.3–0.5
Rotation rate (°/s)	0.3
No. crystals used	5
Total angular rotation collected (°)	383
Merging statistics	
Space group	P2$_1$
Cell dimensions	
a, b, c (Å)	18.78, 4.73, 33.47
α, β, γ (°)	90, 100.02, 90
Resolution (Å)	20–1.5 (1.58–1.50)^a
R_{merge} (%)	22.0 (30.6)
No. reflections	5586 (555)
Unique reflections	1032 (133)
Completeness (%)	91.8 (76.4)
Multiplicity	5.4 (4.2)
I/σ	5.19 (3.11)
CC$_{1/2}$ (%)	98.7 (90.8)
Refinement statistics	
No. reflections	1031
Reflections in test set	103
R_{work} (%)	22.7
R_{free} (%)	29.5
r.m.s. deviations	
Bond lengths (Å)	0.015
Bond angles (°)	1.879
Avg. B factor (Å^2)	
Protein	11.56
Water	14.60
Wilson B factor (Å^2)	7.24
Ramachandran (%)	
Favored	88.9
Allowed	11.1
Outliers	0

^{a} Highest resolution shell shown in parentheses.

wonder how often sequence alignments do not accurately reflect structural alignments.

Additionally, the mated sheets in each of the two atomic structures differ in the number of residues that stabilize Interface A. Ten of the 11 residues of hIAPP(19–29) S20G form Interface A, whereas the same interface of the Aβ(24–34) WT structure is composed of only six of the 11 residues (Fig. 4B). The main reason for the reduced overlap between sheets in the Aβ(24–34) WT atomic structure is that the symmetry axes between sheets lie further from the center of the peptide than in the hIAPP segment structure. The length of this offset is supported by Lys[28], which hydrogen bonds to the carboxyl terminus of its adjacent strand in the mated sheet.

As these atomic structures form the spines of their parent full-length proteins and are so similar, we hypothesized that they could facilitate cross-seeding of amyloid fibril formation. In fact, both Aβ(24–34) WT and hIAPP(19–29) S20G fibrils seeded full-length Aβ(1–42) fibril formation nearly to the efficiency of their cognate full-length protein as seen by thioflavin-T (ThT) fluorescence (Fig. 4C and Fig. S3, A and C). Likewise, both Aβ(24–34) WT and hIAPP(19–29) S20G fibrils seeded full-length hIAPP at similar efficiencies as fibrillar Aβ(1–42), whereas addition of full-length hIAPP seeds is so efficient that initiation of fibrillization occurs immediately (Fig. 4D, Fig. S3, B and D, and supporting methods). These results

suggest that perhaps peptide-based inhibitors of fibril formation, developed for hIAPP using the hIAPP(19–29) S20G atomic structure, may likewise target Aβ.

Development of inhibitors using structure-based design against hIAPP(19–29) S20G

We sought to develop structure-based peptide inhibitors of hIAPP fibril formation using Interface A of the hIAPP(19–29) S20G atomic structure as a scaffold. We used a Rosetta-based design strategy and workflow similar to Sievers *et al.* (47) (Fig. 5A). Our laboratory has used similar strategies to develop peptide-based inhibitors that reduce fibril formation of amyloid proteins tau, p53, and transthyretin, which are implicated in tauopathies, various cancers, and familial amyloid polyneuropathy, respectively (46–48). We performed multiple rounds of design that produced ~50 peptide sequences, about a dozen of which were effective at reducing hIAPP(19–29) S20G fibril formation and cytotoxicity (Table S1 and Figs. S4 and S5).

We chose to focus on two all D-conformation peptide sequences because of their potential for longer *in vivo* stability (49), which may be important during downstream clinical testing (Fig. 5, B and C). These designs, abbreviated p14 and p15, reduced fibril formation of the design target, hIAPP(19–29) S20G (Fig. 5D), at equimolar concentrations, whereas their cognate negative control sequences did not. Consistent with previous findings, reducing fibril formation likewise reduced the cytotoxicity of hIAPP(19–29) S20G to HEK293 cells (Fig. 5E). The peptide-based fibril blockers are specific for the design target; they do not reduce aggregation of three other amyloid proteins, transthyretin, tau, and α-synuclein (Fig. S6 and supporting methods).

Cross-amyloid efficiency of inhibitors

Given the structural and sequence similarity between the two atomic structures and their ability to cross-seed, we aimed to determine whether the inhibitors, developed using the hIAPP(19–29) S20G atomic structure, are effective against both full-length hIAPP and full-length Aβ. Using ThT fluorescence, we observed that p14 and p15 reduced fibril formation of full-length hIAPP, but their cognate negative control peptides (p16 and p17, respectively) did not (Fig. 6A). 48 h into the ThT fluorescence assay in Fig. 6A, the experiment was paused, and aliquots were taken for negative-stain TEM. Negative-stain TEM analysis confirmed the reduction of fibrils in hIAPP samples incubated with p14 and p15. Instead, these samples contained small fibrillar aggregates and amorphous aggregates (Fig. 6B). As expected, hIAPP samples incubated with negative control peptides contained abundant fibrils. Consistent with our observation of reduced fibrils, we observed that p14 and p15 reduced cytotoxicity of full-length hIAPP, but their cognate negative control peptides did not (Fig. 6C). We tested the cytotoxicity of the samples to Rin5F cells, a rat pancreatic β-cell line, and we quantified cytotoxicity using MTT dye reduction. Next, we tested whether the same inhibitors, designed against hIAPP(19–29) S20G, reduce fibril formation and cytotoxicity of full-length Aβ(1–42). We observed that p14 and p15 reduced cytotoxicity of Aβ(1–42) to N2a cells (Fig. 6D), but neither p14 nor p15 appeared to reduce Aβ(1–42) fibril forma-
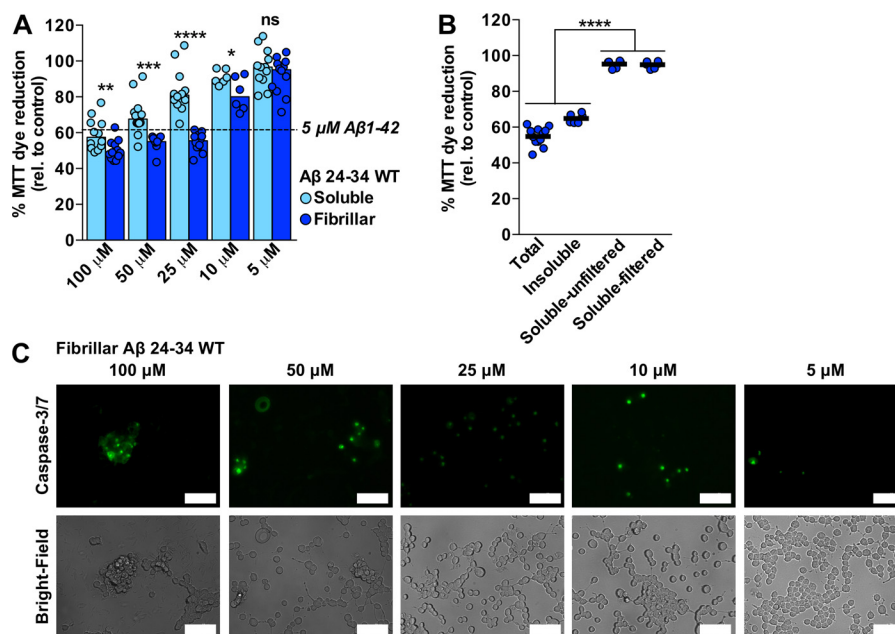
Figure 3. Aβ(24–34) WT is cytotoxic to N2a cells, a mouse neuroblastoma cell line. *A*, the cytotoxicity of Aβ(24–34) WT mainly resides in its fibrillar form, but its soluble form is also mildly cytotoxic. Samples were diluted to 10× from 1 mM stocks and then further diluted 1:10 in medium containing preplated cells to the concentration specified. Concentrations represent monomer equivalents for both preparations. *B*, the insoluble fraction of the 25 μM fibrillar sample, which contains fibrils, is cytotoxic, further confirming that fibrils or some type of oligomer that tightly associates with fibrils is the cytotoxic species. The insoluble fraction was isolated by centrifuging the fibrillar sample for 1 h using a tabletop centrifuge and then aspirating off the soluble fraction. Then the insoluble fraction was resuspended in fresh buffer at its original volume. The "soluble filtered" fraction was filtered with a 0.1-μm spin filter, whereas the "soluble-unfiltered" fraction was not. For *A* and *B*, cytotoxicity was quantified using MTT dye reduction. *Points* and *bars* show median with individual technical replicates ($n = 6–12$; *ns*, not significant; *, $p < 0.05$; **, $p < 0.01$; ***, $p < 0.001$; ****, $p < 0.0001$ using an unpaired *t* test with equal standard deviations (in *A*, relative to vehicle; in *B*, relative as indicated by *brackets*). *C*, the fibrillar form of Aβ(24–34) WT is associated with increased proapoptotic caspase-3/7 activation. Cells were treated as described in *A*, and then caspase-3/7 activity was visualized using a fluorescence-based probe for caspase activity. Cells were imaged using a Zeiss fluorescence microscope. *Scale bars*, 50 μm.

tion (Fig. 6*F*). To investigate whether the peptide inhibitors reduce the formation of some other cytotoxic Aβ(1–42) assemblies, we probed samples with 31 different conformational antibodies. Three monoclonal antibodies, mOC 88, mOC 3, and mOC 22, showed markedly reduced binding to Aβ(1–42) incubated with either p14 or p15 (Fig. 6*E* and Fig. S7). We observed no reduction in binding to Aβ(1–42) incubated with negative control peptides. Although not much is known about the conformations of Aβ that these antibodies recognize, one previous study showed that mOC 3 and mOC 22 bind to Aβ plaques in AD patient–derived brain tissue and bind to hIAPP fibrils formed *in vitro* (50).

In our identification of effective inhibitors, we screened 11 other peptides to test reduction of the cytotoxicity of full-length hIAPP to Rin5F cells (Fig. 7, *A* and *B*). Interestingly, all but one of the peptide inhibitors effective against hIAPP also reduced toxicity of Aβ(1–42) to N2a cells (Fig. 7, *C* and *D*). These seven inhibitors encompass a range of sequences and chemical properties (Fig. 7*C* and Table S1), so we postulate that shape complementarity to the target interface is the primary factor involved in blocking hIAPP or Aβ toxic assembly.

Discussion

As detailed in the Introduction, a variety of biochemical and animal studies have linked Aβ and hIAPP, associated with AD and T2D, respectively, but the underlying cause of the link has not been clear. Previous studies point to their similar sequences and their cross-seeding property *in vivo* and *in vitro* as the

underlying cause (12, 14, 18, 51). Here, through atomic structures determined using microED and designed inhibitors with cross-amyloid efficacy, we provide evidence for a molecular mechanism based on fibril spines having similar structures.

Although the spines of Aβ and hIAPP are similar in sequence and structure, their structural similarity is not fully reflected by their sequence similarity. This is particularly true for the A interfaces of the two segments. This observation that sequence similarity is not a sure determinant of cross-seeding efficiency has been described previously for immunoglobulin (Ig) light chains, polyglutamine tracts, and β_2-microglobulin, all of which seed Aβ(1–40) fibril formation *in vitro* (16), and this is especially true for the amyloid-like prion proteins Sup35p, Ure2p, and Rnq1p (52). The efficiency with which Aβ(24–34) WT and hIAPP(19–29) S20G fibrils seed both Aβ(1–42) and hIAPP fibril formation suggests that their common structures are important for cross-seeding.

Our experiments further support the hypothesis that the linked effects of Aβ(1–42) and hIAPP are based on their similar fibrillar structures; the peptide inhibitors, designed against Interface A of the atomic structure of hIAPP(19–29) S20G, are potent in reducing cytotoxicity of both full-length hIAPP and Aβ(1–42). The mechanism for reducing cytotoxicity of hIAPP in rat pancreatic β-cells appears to involve primarily fibril inhibition. In contrast, the mechanism for reducing Aβ(1–42) cytotoxicity to neuroblastoma cells might involve interference with oligomerization or a relatively small population of fibril
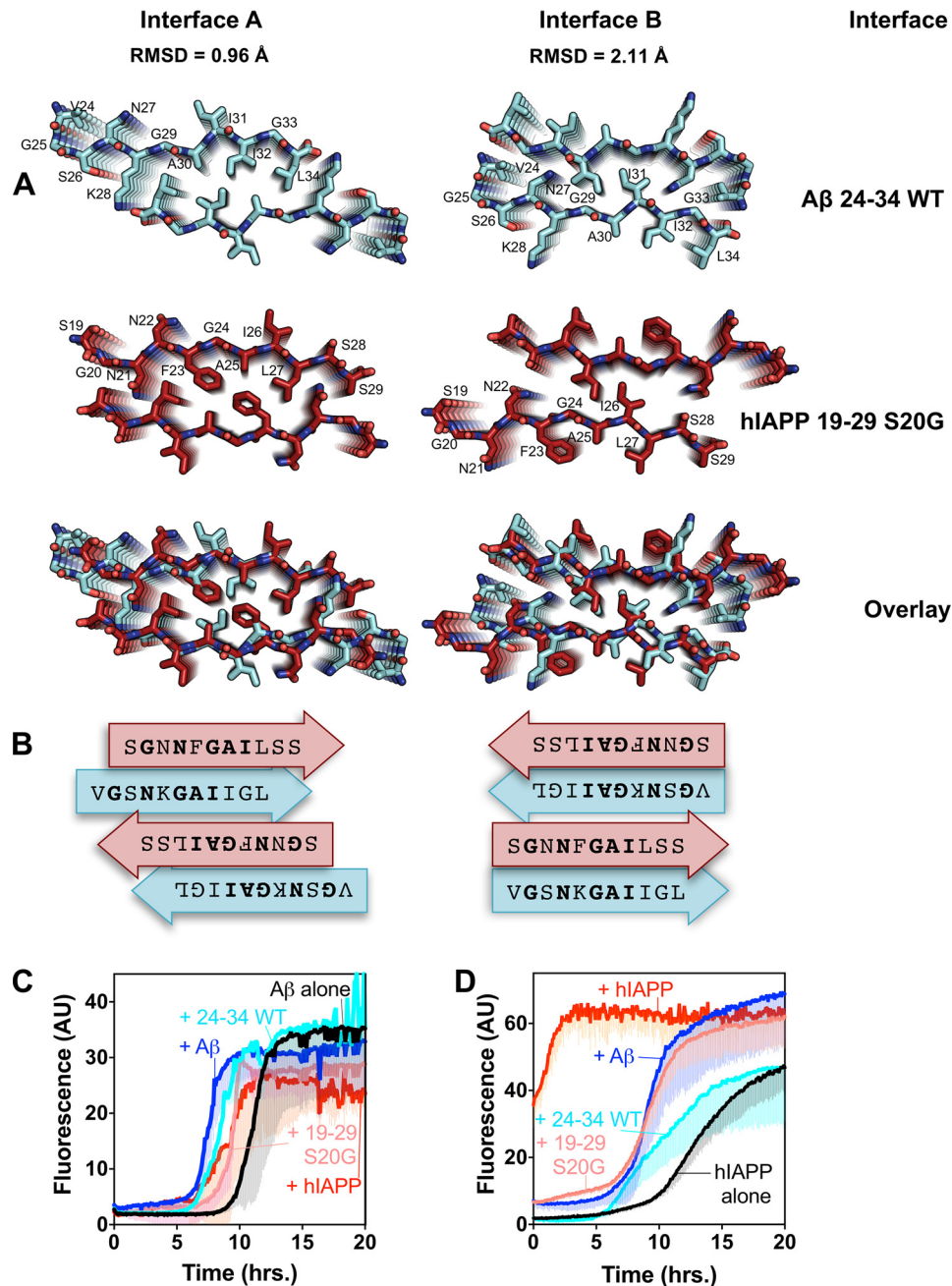
Figure 4. The spines of Aβ(24–34) WT and hIAPP(19–29) S20G are structurally similar. *A*, the crystal packing reveals two interfaces, Interface A and Interface B. The backbone atoms of Interface A (*left*) differ from each other by 0.96-Å r.m.s.d., whereas the backbones of Interface B (*right*) differ from each other by 2.11 Å. r.m.s.d. values were calculated using LSQKAB. *B*, schematic of how superpositions of atomic structures reveal that mated sheets composing Interface A are shifted by two residues and display different degrees of overlap. *C*, seeds of Aβ(24–34) WT and hIAPP(19–29) S20G seed full-length Aβ(1–42) fibril formation at nearly the efficiency of their parent full-length proteins, suggesting that the segments have structures similar to full-length Aβ(1–42) fibrils. *D*, seeds of Aβ(1–42), Aβ(24–34) WT, and hIAPP(19–29) S20G seed full-length hIAPP fibril formation at similar efficacies, whereas hIAPP(1–37) seeds initiate fibrillization immediately. For *C* and *D*, 10 μM Aβ(1–42) or hIAPP was seeded with a 10% (v/v) monomer equivalent of preformed seed of each protein or protein segment. Fluorescence of buffer alone is show in *gray*. *Lines* show the average of three technical replicates with one standard deviation. *AU*, absorbance units.

polymorphs with an interface similar to Interface A observed in the Aβ(24–34) WT structure. The persistence of Aβ fibrils in the presence of inhibitor could be explained by dominance of a less toxic but more prevalent polymorph such as one driven by Aβ [16]KLVFFA[21] ([53]), which we presume would not interact with our inhibitor.

To determine how Aβ(24–34) WT and hIAPP(19–29) S20G may cross-seed, we generated models of all 12 possible heteroassemblies using the structures of these two segments and
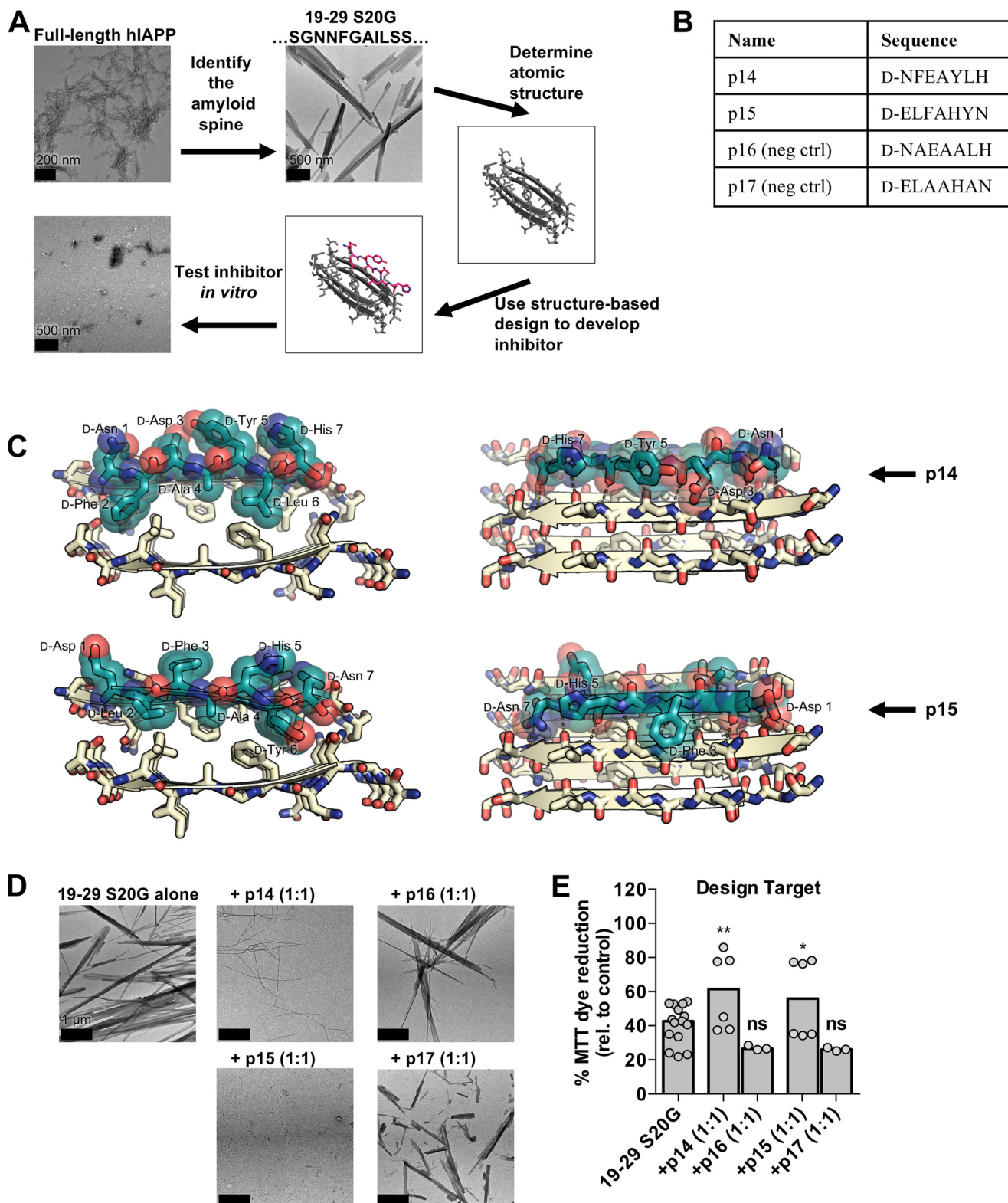
an ideal β-strand as templates. Next, we applied Rosetta to assess their propensities to form. Heteroassemblies constructed using the B interfaces provided several usable models, whereas all heteroassemblies of Interface A failed to converge due to significant steric clashes. The heteroassembly modeled onto the backbone of Interface B of the hIAPP(19–29) S20G atomic structure possesses the highest Sc of all the models at 0.66 (Fig. 8). Its Sc score and Rosetta energy score are comparable with those of the homoassemblies containing Interface B

(Table S2), suggesting that this heteroassembly model may represent an actual interface between Aβ and hIAPP.

This heteroassembly model, taken together with the effects of the inhibitors on hIAPP and Aβ(1–42) fibril formation and cytotoxicity, leads us to suggest that different fibrillar interfaces may be important for cytotoxicity and cross-seeding. Recall

that the inhibitors were designed to target Interface A of the hIAPP(19–29) S20G atomic structure. Indeed, these inhibitors reduced fibril formation and cytotoxicity of full-length hIAPP, likely by targeting a similar interface in the full-length protein and preventing it from forming. In contrast, these inhibitors did not reduce fibril formation of Aβ(1–42), but they did reduce its

Name	Sequence
p14	D-NFEAYLH
p15	D-ELFAHYN
p16 (neg ctrl)	D-NAEAALH
p17 (neg ctrl)	D-ELAAHAN

cytotoxicity. As $A\beta(24-34)$ WT contains a structurally similar Interface A, it seems plausible that these inhibitors target and reduce the formation of interfaces similar to Interface A in both full-length proteins and that Interface A may be important for cytotoxicity of both proteins. Conformation-specific antibodies mOC 88, mOC 3, and mOC 22, all of which show a marked reduction in binding to $A\beta(1-42)$ incubated with inhibitors, may recognize a structural motif, or epitope, similar to Interface A. Indeed, a previous study showed that mOC 3 and mOC 22 recognize epitopes shared between $A\beta$ and hIAPP fibrils (50). The acceptable fit of the heteroassembly model in Fig. 7 suggests that the Interface B of both proteins is important for cross-seeding.

The fibrillar atomic structures of the segments studied here possess structural motifs important for cytotoxicity and cross-seeding, and they may also support the same properties in their parent full-length proteins. Going forward, these structures may serve as templates for the development of pharmaceutical therapeutics that may have dual efficacy.

Experimental procedures

Peptide preparation

Candidate inhibitors were custom-made and purchased from Innopep (San Diego, CA). For studies with the design target, hIAPP(19–29) S20G, lyophilized candidate inhibitors were dissolved at 1 mM in PBS and 1% DMSO. For studies with full-length hIAPP and $A\beta(1-42)$, lyophilized candidate inhibitors were dissolved at 10 mM in 100% DMSO. 10 mM stocks were diluted as necessary. All stocks were stored frozen at −20 °C.

hIAPP(1–37)-NH₂ (hIAPP) was purchased from Innopep. Mouse (m) IAPP(1–37)NH₂ was purchased from CSBio (Menlo Park, CA). Peptides were prepared by dissolving lyophilized peptide in 100% 1,1,1,3,3,3-hexafluoro-2-propanol (HFIP) at 250 μM for 2 h. Next, the sample was spin-filtered, and then HFIP was removed with a CentriVap concentrator (Labconco, Kansas City, MO). After removal of the HFIP, the peptides were dissolved at 1 or 10 mM in 100% DMSO (IAPP alone) or 100% DMSO solutions containing 1 or 10 mM inhibitor. The DMSO peptide stocks were diluted 100-fold in filter-sterilized Dulbecco's PBS (catalog number 14200-075, Life Technologies).

Recombinant amyloid-β peptide cloning and expression

$A\beta$ was cloned and purified similarly to the methods described in Laganowsky et al. (69). $A\beta$ was cloned into p15-maltose-binding protein (MBP) as described previously and expressed with the following exceptions. An overnight starter culture was grown in 100 ml instead of 50 ml, 15 ml (instead of 7 ml) of which was used to inoculate 1 liter. After induction, cells were allowed to grow for 3–4 h at 37 °C (instead of 34 °C). Cells were then harvested by centrifuging at 5,000 × g. The cell pellet was frozen and stored at −80 °C.

The cell pellet was thawed on ice and resuspended in buffer A (50 mM sodium phosphate, 0.3 M sodium chloride, 20 mM imidazole, pH 8.0) at 120 ml per 3 liters of culture volume and lysed by sonication. Crude cell lysate was clarified by centrifugation at 15,000 × g for 30 min at 4 °C. The clarified cell lysate was filtered through a 0.45-μm syringe filtration device (HPF Millex-HV, Millipore, Billerica, MA) before loading onto two 5-ml HisTrap-HP columns (GE Healthcare). The HisTrap-HP column was washed with 5 column volumes of buffer A and then washed in 5 column volumes of 10% buffer B (50 mM sodium phosphate, 0.3 M sodium chloride, 500 mM imidazole, pH 8.0). Protein was eluted in 3 column volumes of 100% buffer B. The pooled sample was diluted to less than 10 mg/ml, loaded into 6,000–8,000 molecular weight–cutoff tubing (Fisher Scientific), and dialyzed against buffer C (25 mM Tris, pH 8.0, 20 mM imidazole, 100 mM sodium chloride) at 4 °C for 4 h, changing buffer after 2 h. The dialyzed sample was pooled, and ¹⁄₅₀ volume of tobacco etch virus protease stock was added. The tobacco etch virus protease reaction was incubated overnight at 4 °C before loading over a 5-ml HisTrap-HP column equilibrated in buffer A. The flow-through, containing the recombinant $A\beta$ peptide, was collected. Pooled recombinant $A\beta$ peptide was filtered through a 0.22-μm filter unit (Steriflip, Millipore) and further purified by reverse-phase high-performance liquid chromatography (HPLC) on a 21.2 × 250-mm Agilent 897250–106 Zorbax StableBond 300 C_8 PrepHT cartridge with 7-μm beads at 80 °C equilibrated in buffer RA (0.1% trifluoroacetic acid (TFA), water) and eluted over a linear gradient from 15 to 50% buffer RB (acetonitrile, 0.1% TFA) in 59 min at a flow rate of 10 ml/min. Absorbances at 220 and 280 nm were recorded using a Waters 2487 dual λ absorbance detector. Peak fractions containing peptide were assessed for purity by MALDI-TOF mass spectrometry (Voyager-DE-STR, Applied Biosystems, Carlsbad, CA). Pooled fractions were frozen in liquid nitrogen and lyophilized. Dried peptide powders were stored in desiccant jars at −20 °C.

Crystallization

²⁴VGSNKGAIIGL³⁴ ($A\beta(24-34)$ WT) was dissolved at 7.5 mg/ml in 25 mM citric acid, pH 4.0, 5% DMSO. Microcrystals were grown in batch at 37 °C with shaking. Crystals grew within 2 days to a maximum of 1 week.

Figure 5. Development of inhibitors using structure-based design against hIAPP(19–29) S20G. *A*, schematic of structure-based design process using RosettaDesign (47). Segment hIAPP(19–29) S20G, which forms the toxic spine of hIAPP, was used as the design target. *B*, overview of peptide inhibitors used in this study and their sequences. Peptides p16 and p17 are the negative controls for peptide inhibitors p14 and p15, respectively. *C*, models of peptide inhibitors p14 and p15 (*dark teal*) bound to the design target, hIAPP(19–29) S20G (*ivory*). The side chains of the peptide inhibitors form hydrophobic interactions with the core of hIAPP(19–29) S20G. Additionally, the peptide inhibitors form hydrogen bonds along the peptide backbone (*left panel*). *D*, designed peptide inhibitors p14 and p15 reduce fibril formation of the design target, hIAPP(19–29) S20G, but negative control peptides do not. 1 mM hIAPP(19–29) S20G was incubated with equimolar concentrations of each inhibitor overnight under quiescent conditions. Fibril abundance was evaluated using TEM. Images were captured at 3,200×. *Scale bars*, 1 μm. *E*, peptide inhibitors reduce cytotoxicity of the design target, hIAPP(19–29) S20G, but negative control (*neg ctrl*) peptides do not. Samples were prepared as described in *D* and then applied to HEK293 cells at 10 μM final concentration for 24 h. Cytotoxicity was quantified using MTT dye reduction. *Columns* show median with individual technical replicates ($n = 3$–6; *ns*, not significant; **, $p = 0.0014$; *, $p = 0.0118$ using an ordinary one-way ANOVA relative to the *leftmost column*).
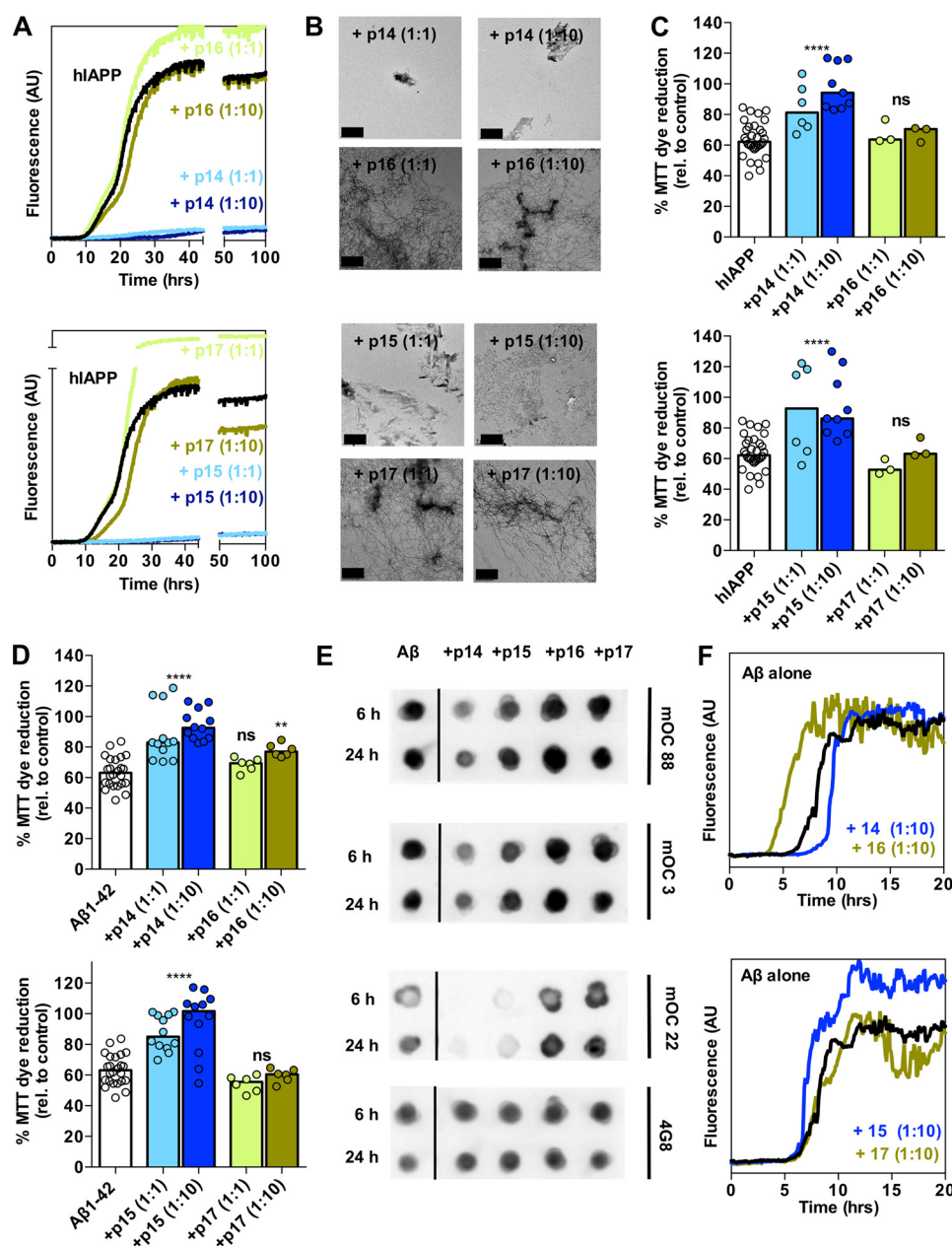
Figure 6. Cross-amyloid efficacy of inhibitors developed with structure-based design against hIAPP(19–29) S20G. *A*, peptide inhibitors p14 and p15 reduce fibril formation of full-length hIAPP, whereas negative control peptides p16 and p17 do not. 10 μM hIAPP was incubated with a 1:1 or 1:10 molar ratio of each inhibitor under quiescent conditions. Fibril formation was monitored using ThT fluorescence. *Lines* show the average of three technical replicates. *B*, negative-stain TEM analysis confirms the results of the ThT assays in *A*. 45 h into the ThT assay, the experiment was paused, and samples were extracted for TEM analysis. After samples were extracted, the assay was resumed for 3 more days. *C*, peptide inhibitors reduce cytotoxicity of full-length hIAPP. 10 μM hIAPP was incubated alone or with the designated concentration of peptide inhibitor overnight under quiescent conditions and then diluted 1:10 with preplated Rin5F cells, a rat pancreatic β-cell line. Cytotoxicity was quantified using MTT dye reduction. *Bars* show median with individual technical replicates ($n = 3$–9; *ns*, not significant; ****, $p < 0.0001$ using an ordinary one-way ANOVA relative to the *leftmost column*). *D*, peptide inhibitors reduce the cytotoxicity of Aβ(1–42), whereas negative control peptides do not. 10 μM Aβ(1–42) was incubated alone or with 1:1 or 1:10 molar ratio of each peptide for 6 h and then diluted 1:10 with preplated N2a cells. Cytotoxicity was quantified using MTT dye reduction. *Bars* represent median with individual technical replicates ($n = 3$–9; *ns*, not significant; ****, $p < 0.0001$ using an ordinary one-way ANOVA relative to the *leftmost column*). *E*, peptide inhibitors reduce the formation of Aβ(1–42) assemblies recognized by conformational monoclonal antibodies, whereas negative control peptides do not. 10 μM Aβ(1–42) was incubated alone (*leftmost column*) or with a 10-fold molar excess of each peptide-based inhibitor. Aliquots of the reaction were tested for antibody binding at 6 and 24 h. Binding to 4G8, a monoclonal antibody specific for residues 17–24 in the linearized Aβ sequence, was used to confirm equal loading of sample onto membranes. Membranes were spliced as indicated for clarity. *F*, peptide inhibitors do not reduce Aβ(1–42) fibril formation as assessed with ThT fluorescence. *AU*, absorbance units.

MicroED data collection

The procedures for microED data collection and processing largely followed published procedures (36, 54). Briefly, a 2–3-μl drop of crystals in suspension was deposited onto a Quantifoil holey-carbon EM grid, then blotted, and vitrified by plunging into liquid ethane using a Vitrobot Mark IV (FEI, Hillsboro, OR). Blotting times and forces were optimized to keep a desired concentration of crystals on the grid and to avoid damaging the crystals. Frozen grids were then either immediately transferred to liquid nitrogen for storage or placed into a Gatan 626 cryo-
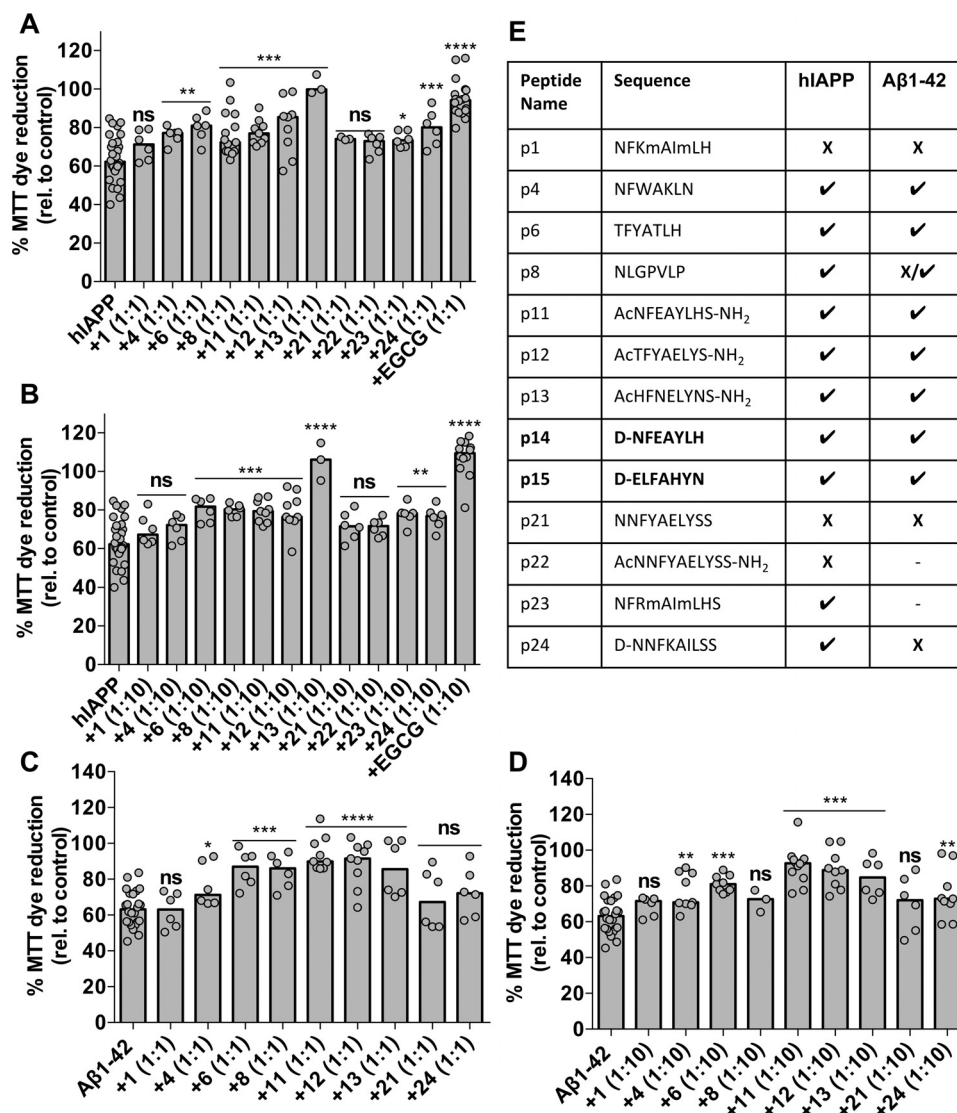
Figure 7. Other peptide inhibitors developed against hIAPP(19–29) S20G reduce cytotoxicity. *A* and *B*, 10 μM hIAPP was incubated alone or with a 1:1 or 1:10 molar ratio of peptide inhibitor overnight under quiescent conditions and then diluted 1:10 with preplated Rin5F cells, a rat pancreatic β-cell line. Cytotoxicity was quantified using MTT dye reduction. *Bars* show mean with one standard deviation ($n = 3-9$; *ns*, not significant; *, $p < 0.05$; **, $p < 0.01$; ***, $p < 0.001$; ****, $p < 0.0001$ using an ordinary one-way ANOVA relative to the *leftmost column*). *C* and *D*, 10 μM Aβ(1–42) was incubated alone or with a 1:1 or 1:10 molar ratio of each peptide for 6 h and then diluted 1:10 with preplated N2a cells. Cytotoxicity was quantified using MTT dye reduction. *Bars* represent median with individual technical replicates ($n = 3-9$; *ns*, not significant; *, $p < 0.05$; **, $p < 0.01$; ***, $p < 0.001$; ****, $p < 0.0001$ using an ordinary one-way ANOVA relative to the *leftmost column*). *E*, summary of peptide inhibitors and efficacies on reduction of cytotoxicity described in this study.

holder for imaging. Images and diffraction patterns were collected from crystals using FEI Tecnai 20 TEM with field emission gun operating at 200 kV and fitted with a bottom mount Tietz Video and Image Processing Systems TemCam-F416 complementary metal oxide semiconductor–based camera. Diffraction patterns were recorded by operating the detector in a video mode using electronic rolling shutter with 2×2 pixel binning (38). Exposure times for these images were either 2 or 3 s/frame. During each exposure, crystals were continuously unidirectionally rotated within the electron beam at a fixed rate of 0.3°/s, corresponding to a fixed angular wedge of 0.6 or 0.9°/frame.

Crystals that appeared visually undistorted produced the best diffraction. Data sets from individual crystals were merged to improve completeness and redundancy. Each crystal data set spanned a wedge of reciprocal space ranging from 40 to 80°. We

used a selected area aperture with an illuminating spot size of ~1 μm. The geometry detailed above equates to an electron dose rate of less than 0.01 e−/Å²/s deposited onto our crystals.

Measured diffraction images were converted from TIFF format into SMV crystallographic format using publicly available software (available for download at http://cryoem.janelia.org/downloads).[4] We used XDS to index the diffraction images and XSCALE (55) for merging and scaling together data sets originating from five different crystals.

Structure determination

We determined the structure of Aβ(24–34) WT using molecular replacement. An idealized 10-residue peptide strand

---

[4] Please note that the JBC is not responsible for the long-term archiving and maintenance of this site or any other third party-hosted site.
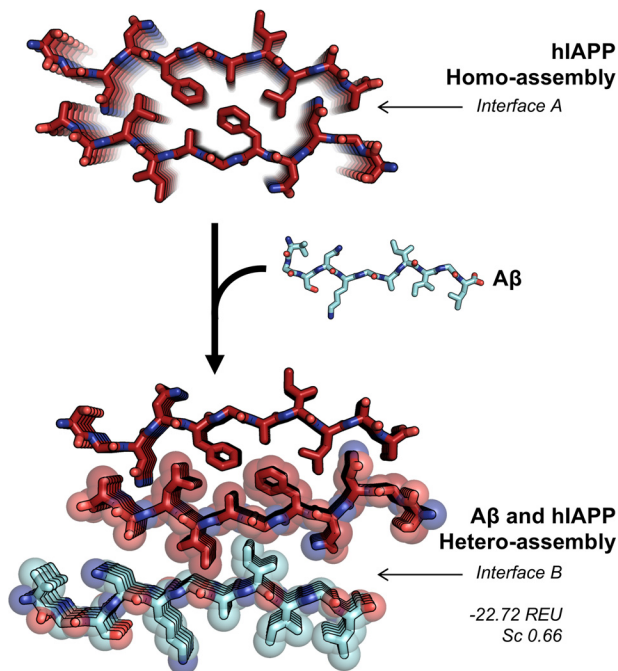
Common fibrillar spines of Aβ and hIAPP

Figure 8. Model of an Aβ(24–34) WT and hIAPP(19–29) S20G heteroassembly, which may explain how full-length Aβ and hIAPP cross-seed. The interface of the heteroassembly model is highlighted with *transparent spheres* representing van der Waals radii. The model was generated from the backbone of Interface B of the hIAPP(19–29) S20G atomic structure using Rosetta. Its Rosetta energy and shape complementarity scores are shown to its *right*. These scores are comparable with the Interface B homoassemblies (Aβ(24–34) WT: −19.4 Rosetta energy units (*REU*); Sc, 0.85; hIAPP(19–29) S20G: −35.09 Rosetta energy units; Sc, 0.72). Our results with the peptide inhibitors suggest that Interface A may be important for cytotoxicity.

with the sequence GAAGAIIGA led us to our atomic model. The solution was identified using Phaser (56). Subsequent rounds of model building and refinement were carried out using Coot and Phenix, respectively (57, 58). Electron scattering factors were used for refinement. Some reflections extended to 1.42-Å resolution. Although the outer shell was incomplete (48% complete), we retained this data as being potentially helpful in the refinement. Statistics are reported to 1.5-Å resolution where completeness reaches 75% (59). Calculations of the buried area and shape complementarity were performed with AREAIMOL (60, 61) and Sc (62–64), respectively.

Fibril diffraction

Fibrils of Aβ(1–42) or microcrystals of Aβ(24–34) WT were spun down and washed with water three times to remove any salt using a tabletop microcentrifuge. The samples were concentrated 20× in water and applied between two capillary ends, and then the samples were left to dry overnight. Fibrils were analyzed with a Rigaku R-AXIS HTC imaging plate detector using CuK$_\alpha$ radiation from a FRE+ rotating anode generator with VARIMAX HR confocal optics (Rigaku, Tokyo, Japan). Radial profiles were calculated using a program written in-house. The program calculates the average intensity as a function of distance from the beam center.

Atomic structure overlay

A structural superposition of Aβ(24–34) WT and hIAPP(19–29) S20G was performed using LSQKAB from the CCP4 suite (65). We calculated r.m.s.d. of main chains.

Computational structure-based design

Computational designs were carried out using the Rosetta-Design software as described previously (47). The atomic structure of the [19]SGNNFGAILSS[29] hIAPP segment was used as a starting template for computational design. An extended L-peptide (or D-peptide; seven to nine residues) was first placed at either the top or bottom of the starting template of the hIAPP(19–29) S20G atomic structure. The design procedure then built side-chain rotamers of all residues onto the nine-residue peptide backbone placed at the growing end of the fibril. The optimal set of rotamers was identified as those that minimize an energy function containing a Lennard-Jones potential, an orientation-dependent hydrogen bond potential, a solvation term, amino acid–dependent reference energies, and a statistical torsional potential that depends on the backbone and side-chain dihedral angles. Buried area and shape complementarity calculations were performed with AREAIMOL and Sc, respectively, from the CCP4 suite of crystallographic programs (60). The solubility of each peptide was evaluated by hydropathy index (66), and its aggregation propensity was calculated by self-stacking score.[5] The designed peptides were selected based on calculated binding energy of top or bottom binding mode, shape complementarity, and peptide solubility. Each structural model of selected peptides went through human inspection using PyMOL where those peptides with sequence redundancy and fewer binding interactions were omitted. Finally, selected peptides were synthesized and tested experimentally.

Testing of candidate inhibitors with design target

To test whether the candidate inhibitors prevent fibril formation of the design target, hIAPP(19–29) S20G, we dissolved the lyophilized hIAPP(19–29) S20G peptide at 1 mM in PBS and 1% DMSO or in an equimolar solution of candidate inhibitor in PBS and 1% DMSO. Samples were incubated for 6–15 h at room temperature under quiescent conditions. Fibril abundance was checked using electron microscopy. Next, the samples were applied to preplated HEK293 cells for 24 h, and then cell viability was measured using MTT dye reduction.

Transmission electron microscopy

Samples were spotted onto non-holey grids and left for 160–180 s. Remaining liquid was wicked off and then left to dry before analyzing. Samples for negative-stain TEM were treated with 2% uranyl acetate after the sample was wicked off the grid. After 1 min, the uranyl acetate was wicked off. The grids were analyzed using a T12 electron microscope (FEI). Images were collected at 3,200× or 15,000× magnification and recorded using a Gatan 2,000 × 2,000 charge-coupled device camera.

ThT kinetic assays

ThT assays with hIAPP were performed in black 384-well plates (Nunc, Rochester, NY) sealed with UV optical tape. hIAPP(1–37)-NH$_2$ and mIAPP(1–37)-NH$_2$ were prepared as

---

[5] L. Jiang *et al.*, unpublished data.

SASBMB

described. The total reaction volume was 50 μl/well. ThT fluorescence was recorded with excitation and emission of 444 and 482 nm, respectively, using a Varioskan Flash (Thermo Fisher Scientific, Grand Island, NY). Experiments were performed at 25 °C without shaking in triplicate, and readings were recorded every 5 min.

For the seeding assays in Fig. 4, 1 mM hIAPP(1–37)-NH$_2$ in 100% DMSO was diluted 1:100 in 0.1 M NaOAc, pH 6.5, containing 10% monomer-equivalent seed and 10 μM ThT. Seeds of Aβ, Aβ(24–34) WT, and hIAPP(19–29) S20G were sonicated for 5 min prior to addition; seeds of hIAPP were not sonicated.

For the inhibition assays in Fig. 6, 1 mM hIAPP(1–37)-NH$_2$ in 100% DMSO was diluted 1:100 in PBS buffer containing 10 μM ThT. Stocks of each inhibitor were diluted 1:100 in the same manner.

ThT assays with Aβ were performed as above with the following exceptions. Experiments were performed in black 96-well plates (Nunc) sealed with UV optical tape. The total reaction volume was 180 μl/well. Experiments were performed at 37 °C without shaking in triplicate, and readings were recorded every 5 min.

For seeding experiments, 1 mM Aβ in 100% DMSO was diluted 1:100 in PBS containing 10% monomer-equivalent seed and 10 μM ThT. Seeds of Aβ, Aβ(24–34) WT, and hIAPP(19–29) S20G were sonicated for 5 min prior to addition; seeds of hIAPP were not sonicated.

For inhibition experiments, 1 mM Aβ in 100% DMSO was diluted 1:100 in PBS containing 25 μM ThT. Stocks of each inhibitor were diluted 1:100 in the same manner.

Cell culture

HEK293 cells were a gift from Carol Eng in the laboratory of Arnold J. Berk at UCLA. Cells were cultured in DMEM (catalog number 11965-092, Life Technologies) plus 10% heat-inactivated fetal bovine serum and 1% penicillin-streptomycin (Life Technologies). Cells were cultured at 37 °C in a 5% CO$_2$ incubator.

Rin5F cells were purchased from ATCC (catalog number CRL-2058; Manassas, VA). Cells were cultured in RPMI 1640 medium (catalog number 30-2001, ATCC) plus 10% heat-inactivated fetal bovine serum. Cells were cultured at 37 °C in a 5% CO$_2$ incubator.

N2a cells were a gift from Pop Wongpalee in the laboratory of Douglas Black at UCLA. Cells were cultured in minimum Eagle's medium (catalog number 11095-080, Life Technologies) plus 10% heat-inactivated fetal bovine serum and 1% penicillin-streptomycin. Cells were cultured at 37 °C in a 5% CO$_2$ incubator.

MTT dye reduction assay for cell viability

HEK293 cells, Rin5F cells, and N2a cells were plated at 10,000, 27,000, and 15,000 cells/well in 90 μl, respectively, in clear 96-well plates (catalog number 3596, Costar, Tewksbury, MA). Cells were allowed to adhere to the plate for 20–24 h. For cell assays with Aβ(24–34) WT, fibrillar samples were incubated for at least 4 days, and soluble samples were freshly dissolved and then applied to N2a cells. For cell assays with the design target, hIAPP(19–29) S20G, samples were incubated

with or without inhibitors for 6–15 h and then applied to HEK293 cells. For cell assays with full-length hIAPP, samples were incubated with or without inhibitors for 15 h to 1 week and then applied to Rin5F cells. For cell assays with Aβ(1–42), samples were incubated with or without inhibitors for 6 h at 37 °C and then applied to N2a cells. 10 μl of sample was added to cells. By doing this, samples were diluted 1:10 from *in vitro* stocks. Experiments were done in triplicate.

After a 24-h incubation, 20 μl of MTT dye (Sigma) was added to each well and incubated for 3.5 h at 37 °C under sterile conditions. The MTT dye stock was 5 mg/ml in Dulbecco's PBS. Next, the plate was removed from the incubator, and the MTT assay was stopped by carefully aspirating off the culture medium and adding 100 μl of 100% DMSO to each well. Absorbance was measured at 570 nm using a SpectraMax M5. A background reading was recorded at 700 nm and subsequently subtracted from the 570 nm value. Cells treated with vehicle alone (PBS + 0.1% DMSO) were designated at 100% viable, and cell viability of all other treatments was calculated accordingly.

We determined the appropriate statistical test for significance by assessing whether 1) the sample sets had a Gaussian distribution using a D'Agostino-Pearson omnibus normality test and 2) the sample sets had equal variance using a Bartlett's test or F test. For samples with Gaussian distributions and equal variances, we used an unpaired *t* test with equal standard deviations. For samples with Gaussian distributions but unequal variances, we used an unpaired *t* test with Welch's correction. For samples with non-Gaussian distributions and unequal variances, we used a Mann-Whitney U test.

Detection of caspase-3/7

N2a cells were plated at 7,200 cells/well in black-walled 96-well plates (catalog number 3603, Costar) and treated as described in the previous section. After a 24-h treatment, cell medium was aspirated, and then 100 μl of 2 μM Nexcelom ViaStain Live Caspase 3/7 in PBS (catalog number CSK-V0003-1, Nexcelom Bioscience LLC, Lawrence, MA) was added to each well. The stain was incubated with cells at 37 °C for 30 min, and then the cells were imaged using a Celigo Image Cytometer (Nexcelom Bioscience) and a Zeiss fluorescence microscope. Cells treated with 2 μM staurosporine were used as a positive control for caspase activation.

Heteroassembly model

Energies and structures for the heteroassembly models were calculated using the 3D profile method (67). Using Rosetta, the sequences of Aβ(24–34) WT and hIAPP(19–29) S20G were "threaded" onto three template backbone structures: the Aβ(24–34) WT backbone, the hIAPP(19–29) S20G fiber backbone, and an idealized β-sheet fiber backbone. The distance between the β-sheets of each of these threaded structures was varied by 10 Å in increments of 0.25 Å, and the shift along the stand axis was 20 Å, also by 0.25-Å increments. Each of the structures was scored by Rosetta energy, buried surface area, and shape complementarity (68).

ASBMB

J. Biol. Chem. (2018) 293(8) 2888–2902 **2899**

Dot blot assay

Aβ(1–42) samples were incubated at 10 μM with or without inhibitors for 6 and 24 h at 37 °C and spotted onto a nitrocellulose membrane (catalog number 162-0146, Bio-Rad). 20 μl was loaded for each condition; 2 μl was spotted at a time and allowed to dry between applications. The membranes were blotted as described previously (35) with the exception of the primary antibodies used. The antibodies used in the assay were generated and characterized previously (50).

References

1. Eisenberg, D., and Jucker, M. (2012) The amyloid state of proteins in human diseases. *Cell* **148,** 1188–1203 CrossRef Medline
2. Sunde, M., Serpell, L. C., Bartlam, M., Fraser, P. E., Pepys, M. B., and Blake, C. C. (1997) Common core structure of amyloid fibrils by synchrotron X-ray diffraction. *J. Mol. Biol.* **273,** 729–739 CrossRef Medline
3. Rodriguez, J. A., Ivanova, M. I., Sawaya, M. R., Cascio, D., Reyes, F. E., Shi, D., Sangwan, S., Guenther, E. L., Johnson, L. M., Zhang, M., Jiang, L., Arbing, M. A., Nannenga, B. L., Hattne, J., Whitelegge, J., *et al.* (2015) Structure of the toxic core of α-synuclein from invisible crystals. *Nature* **525,** 486–490 CrossRef Medline
4. Cooper, G. J., Willis, A. C., Clark, A., Turner, R. C., Sim, R. B., and Reid, K. B. (1987) Purification and characterization of a peptide from amyloid-rich pancreases of type 2 diabetic patients. *Proc. Natl. Acad. Sci. U.S.A.* **84,** 8628–8632 CrossRef Medline
5. Westermark, P., Wernstedt, C., Wilander, E., Hayden, D. W., O'Brien, T. D., and Johnson, K. H. (1987) Amyloid fibrils in human insulinoma and islets of Langerhans of the diabetic cat are derived from a neuropeptide-like protein also present in normal islet cells. *Proc. Natl. Acad. Sci. U.S.A.* **84,** 3881–3885 CrossRef Medline
6. Morales, R., Moreno-Gonzalez, I., and Soto, C. (2013) Cross-Seeding of misfolded proteins: implications for etiology and pathogenesis of protein misfolding diseases. *PLoS Pathog.* **9,** e1003537 CrossRef Medline
7. Guo, J.-P., Arai, T., Miklossy, J., and McGeer, P. L. (2006) Aβ and tau form soluble complexes that may promote self aggregation of both into the insoluble forms observed in Alzheimer's disease. *Proc. Natl. Acad. Sci. U.S.A.* **103,** 1953–1958 CrossRef Medline
8. Uéda, K., Fukushima, H., Masliah, E., Xia, Y., Iwai, A., Yoshimoto, M., Otero, D. A., Kondo, J., Ihara, Y., and Saitoh, T. (1993) Molecular cloning of cDNA encoding an unrecognized component of amyloid in Alzheimer disease. *Proc. Natl. Acad. Sci. U.S.A.* **90,** 11282–11286 CrossRef Medline
9. Buxbaum, J. N., Ye, Z., Reixach, N., Friske, L., Levy, C., Das, P., Golde, T., Masliah, E., Roberts, A. R., and Bartfai, T. (2008) Transthyretin protects Alzheimer's mice from the behavioral and biochemical effects of Aβ toxicity. *Proc. Natl. Acad. Sci. U.S.A.* **105,** 2681–2686 CrossRef Medline
10. Westermark, P., Li, Z. C., Westermark, G. T., Leckström, A., and Steiner, D. F. (1996) Effects of β cell granule components on human islet amyloid polypeptide fibril formation. *FEBS Lett.* **379,** 203–206 CrossRef Medline
11. Wiltzius, J. J., Sievers, S. A., Sawaya, M. R., and Eisenberg, D. (2009) Atomic structures of IAPP (amylin) fusions suggest a mechanism for fibrillation and the role of insulin in the process. *Protein Sci.* **18,** 1521–1530 CrossRef Medline
12. Oskarsson, M. E., Paulsson, J. F., Schultz, S. W., Ingelsson, M., Westermark, P., and Westermark, G. (2015) *In vivo* seeding and cross-seeding of localized amyloidosis. *Am. J. Pathol.* **185,** 834–846 CrossRef Medline
13. Kapurniotu, A. (2001) Amyloidogenicity and cytotoxicity of islet amyloid polypeptide. *Biopolymers* **60,** 438–459 CrossRef Medline
14. Andreetto, E., Yan, L. M., Tatarek-Nossol, M., Velkova, A., Frank, R., and Kapurniotu, A. (2010) Identification of hot regions of the Aβ-IAPP interaction interface as high-affinity binding sites in both cross- and self-association. *Angew. Chem. Int. Ed. Engl.* **49,** 3081–3085 CrossRef Medline
15. Hu, R., Zhang, M., Chen, H., Jiang, B., and Zheng, J. (2015) Cross-seeding interaction between β-amyloid and human islet amyloid polypeptide. *ACS Chem. Neurosci.* **6,** 1759–1768 CrossRef Medline
16. O'Nuallain, B., Williams, A. D., Westermark, P., and Wetzel, R. (2004) Seeding specificity in amyloid growth induced by heterologous fibrils. *J. Biol. Chem.* **279,** 17490–17499 CrossRef Medline
17. Andreetto, E., Malideli, E., Yan, L. M., Kracklauer, M., Farbiarz, K., Tatarek-Nossol, M., Rammes, G., Prade, E., Neumüller, T., Caporale, A., Spanopoulou, A., Bakou, M., Reif, B., and Kapurniotu, A. (2015) A hot-segment-based approach for the design of cross-amyloid interaction surface mimics as inhibitors of amyloid self-assembly. *Angew. Chem. Int. Ed. Engl.* **54,** 13095–13100 CrossRef Medline
18. Moreno-Gonzalez, I., Edwards, G., III, Salvadores, N., Shahnawaz, M., Diaz-Espinoza, R., and Soto, C. (2017) Molecular interaction between type 2 diabetes and Alzheimer's disease through cross-seeding of protein misfolding. *Mol. Psychiatry.* **22,** 1327–1334 CrossRef Medline
19. Janson, J., Laedtke, T., Parisi, J. E., O'Brien, P., Petersen, R. C., and Butler, P. C. (2004) Increased risk of type 2 diabetes in Alzheimer disease. *Diabetes.* **53,** 474–481 CrossRef Medline
20. Miklossy, J., Qing, H., Radenovic, A., Kis, A., Vileno, B., Làszló, F., Miller, L., Martins, R. N., Waeber, G., Mooser, V., Bosman, F., Khalili, K., Darbinian, N., and McGeer, P. L. (2010) β amyloid and hyperphosphorylated tau deposits in the pancreas in type 2 diabetes. *Neurobiol. Aging* **31,** 1503–1515 CrossRef Medline
21. Peila, R., Rodriguez, B. L., Launer, L. J., and Honolulu-Asia Aging Study (2002) Type 2 diabetes, APOE gene, and the risk for dementia and related pathologies. *Diabetes* **51,** 1256–1262 CrossRef Medline
22. Mukherjee, A., Morales-Scheihing, D., Butler, P. C., and Soto, C. (2015) Type 2 diabetes as a protein misfolding disease. *Trends Mol. Med.* **21,** 439–449 CrossRef Medline
23. Akter, K., Lanza, E. A., Martin, S. A., Myronyuk, N., Rua, M., and Raffa, R. B. (2011) Diabetes mellitus and Alzheimer's disease: shared pathology and treatment? *Br. J. Clin. Pharmacol.* **71,** 365–376 CrossRef Medline
24. Lee, S. C., Hashim, Y., Li, J. K., Ko, G. T., Critchley, J. A., Cockram, C. S., and Chan, J. C. (2001) The islet amyloid polypeptide (amylin) gene S20G mutation in Chinese subjects: evidence for associations with type

2 diabetes and cholesterol levels. *Clin. Endocrinol.* **54,** 541–546 CrossRef

25. Morita, S., Sakagashira, S., Ueyama, M., Shimajiri, Y., Furuta, M., and Sanke, T. (2011) Progressive deterioration of insulin secretion in Japanese type 2 diabetic patients in comparison with those who carry the S20G mutation of the islet amyloid polypeptide gene: A long-term follow-up study. *J. Diabetes Investig.* **2,** 287–292 CrossRef Medline

26. Sakagashira, S., Sanke, T., Hanabusa, T., Shimomura, H., Ohagi, S., Kumagaye, K. Y., Nakajima, K., and Nanjo, K. (1996) Missense mutation of amylin gene (S20G) in Japanese NIDDM patients. *Diabetes* **45,** 1279–1281 Medline

27. Lührs, T., Ritter, C., Adrian, M., Riek-Loher, D., Bohrmann, B., Döbeli, H., Schubert, D., and Riek, R. (2005) 3D structure of Alzheimer's amyloid-β(1–42) fibrils. *Proc. Natl. Acad. Sci. U.S.A.* **102,** 17342–17347 CrossRef Medline

28. Wälti, M. A., Ravotti, F., Arai, H., Glabe, C. G., Wall, J. S., Böckmann, A., Güntert, P., Meier, B. H., and Riek, R. (2016) Atomic-resolution structure of a disease-relevant Aβ(1–42) amyloid fibril. *Proc. Natl. Acad. Sci. U.S.A.* **113,** E4976–E4984 CrossRef Medline

29. Scheidt, H. A., Morgado, I., Rothemund, S., and Huster, D. (2012) Dynamics of amyloid β fibrils revealed by solid-state NMR. *J. Biol. Chem.* **287,** 2017–2021 CrossRef Medline

30. Colvin, M. T., Silvers, R., Ni, Q. Z., Can, T. V., Sergeyev, I., Rosay, M., Donovan, K. J., Michael, B., Wall, J., Linse, S., and Griffin, R. G. (2016) Atomic resolution structure of monomorphic Aβ42 amyloid fibrils. *J. Am. Chem. Soc.* **138,** 9663–9674 CrossRef Medline

31. Colletier, J.-P., Laganowsky, A., Landau, M., Zhao, M., Soriaga, A. B., Goldschmidt, L., Flot, D., Cascio, D., Sawaya, M. R., and Eisenberg, D. (2011) Molecular basis for amyloid-polymorphism. *Proc. Natl. Acad. Sci. U.S.A.* **108,** 16938–16943 CrossRef Medline

32. Fonte, V., Dostal, V., Roberts, C. M., Gonzales, P., Lacor, P. N., Velasco, P. T., Magrane, J., Dingwell, N., Fan, E. Y., Silverman, M. A., Stein, G. H., and Link, C. D. (2011) A glycine zipper motif mediates the formation of toxic β-amyloid oligomers *in vitro* and *in vivo*. *Mol. Neurodegener.* **6,** 61 CrossRef Medline

33. Harmeier, A., Wozny, C., Rost, B. R., Munter, L.-M., Hua, H., Georgiev, O., Beyermann, M., Hildebrand, P. W., Weise, C., Schaffner, W., Schmitz, D., and Multhaup, G. (2009) Role of amyloid-β glycine 33 in oligomerization, toxicity, and neuronal plasticity. *J. Neurosci.* **29,** 7582–7590 CrossRef Medline

34. Kanski, J., Varadarajan, S., Aksenova, M., and Butterfield, D. A. (2002) Role of glycine-33 and methionine-35 in Alzheimer's amyloid β-peptide 1–42-associated oxidative stress and neurotoxicity. *Biochim. Biophys. Acta* **1586,** 190–198 CrossRef Medline

35. Krotee, P., Rodriguez, J. A., Sawaya, M. R., Cascio, D., Reyes, F. E., Shi, D., Hattne, J., Nannenga, B. L., Oskarsson, M. E., Philipp, S., Griner, S., Jiang, L., Glabe, C. G., Westermark, G. T., Gonen, T., *et al.* (2017) Atomic structures of fibrillar segments of hIAPP suggest tightly mated β-sheets are important for cytotoxicity. *Elife* **6,** e19273 CrossRef Medline

36. Hattne, J., Reyes, F. E., Nannenga, B. L., Shi, D., de la Cruz, M. J., Leslie, A. G., and Gonen, T. (2015) MicroED data collection and processing. *Acta Crystallogr. A Found. Adv.* **71,** 353–360 CrossRef Medline

37. Liu, S., Hattne, J., Reyes, F. E., Sanchez-Martinez, S., Jason de la Cruz, M., Shi, D., and Gonen, T. (2017) Atomic resolution structure determination by the cryo-EM method MicroED. *Protein Sci.* **26,** 8–15 CrossRef Medline

38. Nannenga, B. L., Shi, D., Leslie, A. G. W., and Gonen, T. (2014) High-resolution structure determination by continuous-rotation data collection in MicroED. *Nat. Methods* **11,** 927–930 CrossRef Medline

39. Shi, D., Nannenga, B. L., Iadanza, M. G., and Gonen, T. (2013) Three-dimensional electron crystallography of protein microcrystals. *Elife* **2,** e01345 CrossRef Medline

40. Lorenzo, A., and Yankner, B. A. (1996) Amyloid fibril toxicity in Alzheimer's disease and diabetes. *Ann. N.Y. Acad. Sci.* **777,** 89–95 CrossRef Medline

41. Olmsted, J. B., Carlson, K., Klebe, R., Ruddle, F., and Rosenbaum, J. (1970) Isolation of microtubule protein from cultured mouse neuroblastoma cells. *Proc. Natl. Acad. Sci. U.S.A.* **65,** 129–136 CrossRef Medline

42. Mosmann, T. (1983) Rapid colorimetric assay for cellular growth and survival: application to proliferation and cytotoxicity assays. *J. Immunol. Methods.* **65,** 55–63 CrossRef Medline

43. Liu, Y., Peterson, D. A., Kimura, H., and Schubert, D. (1997) Mechanism of cellular 3-(4,5-dimethylthiazol-2-yl)-2,5-diphenyltetrazolium bromide (MTT) reduction. *J. Neurochem.* **69,** 581–593 Medline

44. Pike, C. J., Walencewicz-Wasserman, A. J., Kosmoski, J., Cribbs, D. H., Glabe, C. G., and Cotman, C. W. (1995) Structure-activity analyses of β-amyloid peptides: contributions of the β 25–35 region to aggregation and neurotoxicity. *J. Neurochem.* **64,** 253–265 Medline

45. Yankner, B. A., Duffy, L. K., and Kirschner, D. A. (1990) Neurotrophic and neurotoxic effects of amyloid β protein: reversal by tachykinin neuropeptides. *Science.* **250,** 279–282 CrossRef Medline

46. Saelices, L., Johnson, L. M., Liang, W. Y., Sawaya, M. R., Cascio, D., Ruchala, P., Whitelegge, J., Jiang, L., Riek, R., and Eisenberg, D. S. (2015) Uncovering the mechanism of aggregation of human transthyretin. *J. Biol. Chem.* **290,** 28932–28943 CrossRef Medline

47. Sievers, S. A., Karanicolas, J., Chang, H. W., Zhao, A., Jiang, L., Zirafi, O., Stevens, J. T., Münch, J., Baker, D., and Eisenberg, D. (2011) Structure-based design of non-natural amino-acid inhibitors of amyloid fibril formation. *Nature* **475,** 96–100 CrossRef Medline

48. Soragni, A., Janzen, D. M., Johnson, L. M., Lindgren, A. G., Thai-Quynh Nguyen, A., Tiourin, E., Soriaga, A. B., Lu, J., Jiang, L., Faull, K. F., Pellegrini, M., Memarzadeh, S., and Eisenberg, D. S. (2016) A designed inhibitor of p53 aggregation rescues p53 tumor suppression in ovarian carcinomas. *Cancer Cell* **29,** 90–103 CrossRef Medline

49. Miller, S. M., Simon, R. J., Ng, S., Zuckermann, R. N., Kerr, J. M., and Moos, W. H. (1995) Comparison of the proteolytic susceptibilities of homologous L-amino acid, D-amino acid, and N-substituted glycine peptide and peptoid oligomers. *Drug Dev. Res.* **35,** 20–32 CrossRef

50. Hatami, A., Albay, R., 3rd, Monjazeb, S., Milton, S., and Glabe, C. (2014) Monoclonal antibodies against Aβ42 fibrils distinguish multiple aggregation state polymorphisms in vitro and in Alzheimer disease brain. *J. Biol. Chem.* **289,** 32131–32143 CrossRef Medline

51. Morales, R., Duran-Aniotz, C., Diaz-Espinoza, R., Camacho, M. V., and Soto, C. (2012) Protein misfolding cyclic amplification of infectious prions. *Nat. Protoc.* **7,** 1397–1409 CrossRef Medline

52. Ross, C. D., McCarty, B. R., Hamilton, M., Ben-Hur, A., and Ross, E. D. (2009) A promiscuous prion: efficient induction of [URE3] prion formation by heterologous prion domains. *Genetics* **183,** 929–940 CrossRef Medline

53. Tjernberg, L. O., Näslund, J., Lindqvist, F., Johansson, J., Karlström, A. R., Thyberg, J., Terenius, L., and Nordstedt, C. (1996) Arrest of β-amyloid fibril formation by a pentapeptide ligand. *J. Biol. Chem.* **271,** 8545–8548 CrossRef Medline

54. Shi, D., Nannenga, B. L., de la Cruz, M. J., Liu, J., Sawtelle, S., Calero, G., Reyes, F. E., Hattne, J., and Gonen, T. (2016) The collection of MicroED data for macromolecular crystallography. *Nat. Protoc.* **11,** 895–904 CrossRef Medline

55. Kabsch, W. (2010) XDS. *Acta Crystallogr. D Biol. Crystallogr.* **66,** 125–132 CrossRef Medline

56. McCoy, A. J. (2007) Solving structures of protein complexes by molecular replacement with Phaser. *Acta Crystallogr. D Biol. Crystallogr.* **63,** 32–41 CrossRef Medline

57. Emsley, P., and Cowtan, K. (2004) Coot: model-building tools for molecular graphics. *Acta Crystallogr. D Biol. Crystallogr.* **60,** 2126–2132 CrossRef Medline

58. McCoy, A. J., Grosse-Kunstleve, R. W., Storoni, L. C., and Read, R. J. (2005) Likelihood-enhanced fast translation functions. *Acta Crystallogr. D Biol. Crystallogr.* **61,** 458–464 CrossRef Medline

59. Diederichs, K., and Karplus, P. A. (2013) Better models by discarding data? *Acta Crystallogr. D Biol. Crystallogr.* **69,** 1215–1222 CrossRef Medline

60. Collaborative Computational Project, Number 4 (1994) The CCP4 suite: programs for protein crystallography. *Acta Crystallogr. D Biol. Crystallogr.* **50,** 760–763 CrossRef Medline

61. Lee, B., and Richards, F. M. (1971) The interpretation of protein structures: estimation of static accessibility. *J. Mol. Biol.* **55,** 379–400 CrossRef Medline

62. Connolly, M. L. (1983) Solvent-accessible surfaces of proteins and nucleic acids. *Science* **221,** 709–713 CrossRef Medline

63. Lawrence, M. C., and Colman, P. M. (1993) Shape complementarity at protein-protein interfaces. *J. Mol. Biol.* **234,** 946–950 CrossRef Medline

64. Richards, F. M. (1977) Areas, volumes, packing, and protein structure. *Annu. Rev. Biophys. Bioeng.* **6,** 151–176 CrossRef Medline

65. Kabsch, W. (1976) A solution for the best rotation to relate two sets of vectors. *Acta Crystallogr. A* **32,** 922–923 CrossRef

66. Kyte, J., and Doolittle, R. F. (1982) A simple method for displaying the hydropathic character of a protein. *J. Mol. Biol.* **157,** 105–132 CrossRef Medline

67. Thompson, M. J., Sievers, S. A., Karanicolas, J., Ivanova, M. I., Baker, D., and Eisenberg, D. (2006) The 3D profile method for identifying fibril-forming segments of proteins. *Proc. Natl. Acad. Sci. U.S.A.* **103,** 4074–4078 CrossRef Medline

68. Kuhlman, B., Dantas, G., Ireton, G. C., Varani, G., Stoddard, B. L., and Baker, D. (2003) Design of a novel globular protein fold with atomic-level accuracy. *Science* **302,** 1364–1368 CrossRef Medline

69. Laganowsky, A., Liu, C., Sawaya, M. R., Whitelegge, J. P., Park, J., Zhao, M., Pensalfini, A., Soriaga, A. B., Landau, M., Teng, P. K., Cascio, D., Glabe, C., and Eisenberg, D. (2012) Atomic view of a toxic amyloid small oligomer. *Science* **335,** 1228–1231 CrossRef Medline

ASBMB